

Influence of Near Real-Time Green Vegetation Fraction Data on Numerical Weather Prediction by WRF over North China

Bing LU¹, Jiqin ZHONG^{1*}, Wei WANG², Shihao TANG³, and Zhaojun ZHENG³

¹ Institute of Urban Meteorology, China Meteorological Administration, Beijing 100089, China

² National Center for Atmospheric Research, Boulder, CO 80301, USA

³ Key Laboratory of Radiometric Calibration and Validation for Environmental Satellites, National Satellite Meteorological Center, China Meteorological Administration, Beijing 100089, China

(Received September 22, 2020; in final form February 18, 2021)

ABSTRACT

The green vegetation fraction (GVF) can greatly influence the partitioning of surface sensible and latent heat fluxes in numerical weather prediction (NWP) models. However, the multiyear averaged monthly GVF climatology—the most commonly used representation of the vegetation state in models—cannot capture the real-time vegetation state well. In this study, a near real-time (NRT) GVF dataset generated from an 8-day composite of the normalized difference vegetation index is compared with the 10-yr averaged monthly GVF provided by the WRF model. The annual variability of the GVF over North China is examined in detail. Many differences between the two GVF datasets are found over dryland, grassland, and cropland/grassland mosaic areas. Two experiments using different GVF datasets are performed to assess the impacts of GVF on forecasts of screen-level temperature and humidity. The results show that using NRT GVF can lead to a widespread reduction of 2-m temperature forecast errors from April to October. Evaluation against in-situ observations shows that the positive impact on 2-m temperature forecasts in the morning is more distinct than that in the afternoon. Our study demonstrates that NRT GVF can provide a more realistic representation of the vegetation state, which in turn helps to improve short-range forecasts in arid and semiarid regions of North China. Moreover, our study shows that the negative effect of using NRT GVF is closely related to the initial soil moisture.

Key words: green vegetation fraction (GVF), near real-time (NRT), soil moisture, 2-m temperature and humidity, warm season

Citation: Lu, B., J. Q. Zhong, W. Wang, et al., 2021: Influence of near real-time green vegetation fraction data on numerical weather prediction by WRF over North China. *J. Meteor. Res.*, **35**(3), 505–520, doi: 10.1007/s13351-021-0163-6.

1. Introduction

In global and regional numerical weather prediction (NWP) models, land surface processes can substantially affect weather forecasts at both short and medium ranges (Rowell and Blondin, 1990; Beljaars et al., 1996; Balasamo et al., 2009; Koster et al., 2010; Zheng et al., 2014). Vegetation, together with various other land surface parameters in the land surface model (LSM), such as albedo and roughness, can directly influence the regional weather and climate through biophysical feedbacks, including exchanges of moisture, energy, and momentum

with the atmosphere (Chen and Dudhia, 2001; Ek et al., 2003). The vegetation layer in the LSM plays a central role in the energy exchanges between the land and atmosphere (Abramopoulos, 1988). For instance, vegetation contributes to the evaporation that takes place through plant transpiration, as well as the direct evaporation of the plant-intercepted precipitation (Dickinson et al., 2002). The high sensitivity of the latent heat flux (LH) to the green vegetation fraction (GVF) has been well documented (Miller et al., 2006). LSMS represent the vegetation state by the GVF cover, leaf area index (LAI), or both. Remotely sensed land vegetation indexes are used

Supported by the National Key Research and Development Program of China (2018YFC1506802) and National Natural Science Foundation of China (41705087).

*Corresponding author: jqzhong@ium.cn

© The Chinese Meteorological Society and Springer-Verlag Berlin Heidelberg 2021

to provide the surface vegetation coverage and density globally and seasonally (Gutman and Ignatov, 1998). Estimations of high spatial and temporal resolution GVF products generated from remote sensors have been shown to possess good consistency with in-situ measurements over China (Mu et al., 2021). For instance, the climatological GVF datasets, derived from the NOAA's Advanced Very High Resolution Radiometer, have been used in the operational NWP models of the NCEP (Gutman and Ignatov, 1998; Zeng et al., 2003). Boussetta et al. (2013) introduced a monthly climatology of LAI based on the Moderate Resolution Imaging Spectroradiometer (MODIS) satellite product to the ECMWF Integrated Forecasting System (IFS) by using an optimal interpolation analysis through a combination of satellite observations and derived LAI climatology. In the past few decades, the introduction of satellite-based climatological GVF/LAI products into LSMs has greatly improved weather forecasts.

However, the spatial and temporal patterns of vegetation are affected by the variability of the weather and climate, and the climatological GVF can fail to capture the real-time vegetation state of any particular day or year via a multiyear mean. Since the phenology of the appearances of plants and leaves can change every 3–7 days (Kogan, 1997), the vegetation fraction is known to vary considerably over weeks and seasons, with substantial interannual variability (Zeng et al., 2000; Kurkowski et al., 2003). A study of the phenological information relating to the vegetation of the Tibetan Plateau area showed that the growing season length has been extended owing to the earlier start date of the vegetation growing season (Liu et al., 2020). The monthly timescale is too coarse to accurately characterize the development of vegetation. Real-time vegetation cover has an interannual variability, especially in arid and semiarid areas, where the annual precipitation may vary significantly from year to year.

Thus, the requirement for an accurate representation of the vegetation state in numerical models has yet to be adequately addressed. Many investigations have shown that, when compared to climatological data, the usage of near real-time (NRT) GVF can produce a significant impact on the near-surface atmosphere. For instance, being able to better represent the current vegetation state by updating the NRT GVF on a weekly basis in the Noah LSM has led to improvement in the forecasting of surface soil moisture and temperature (Yin et al., 2016), accurate partitioning of surface sensible and LHS (Crawford et al., 2001; Miller et al., 2006), and forecasts of 2-m temperature and humidity for most of the growing season (Kurkowski et al., 2003; Jiang et al., 2010). NRT GVF can

also modulate the environmental conditions for convection systems, and thus can lead to improvements in the forecasting of precipitation (James et al., 2009; Case et al., 2014) and some extreme climate conditions (Boussetta et al., 2015; Yan et al., 2019).

North China is a vast area with complex topography and diverse vegetation, covering farmland, grassland, and woodland. It is dominated by the midlatitude monsoon climate, and strongly affected by the winter and summer monsoons. The annual and interannual precipitation variations are the key factors for vegetation growth in North China. Abundant rainfall and high temperatures are very beneficial to the growth of plants in the vigorous growth period, usually in spring and summer. The interannual variation of precipitation in North China is generally quite clear, leading to obvious interannual variation of the vegetation growth trend, meaning that the monthly timescale is too coarse to accurately characterize the rapid change in the state of greening and senescence of vegetation, and the multiyear mean is too rough to present the specific vegetation state in a particular dry or wet year. Therefore, much attention has been paid to the interactions between regional climate and vegetation over China, with numerous studies having investigated how dynamic vegetation properties can affect the regional climate (Ge et al., 2014; Yan et al., 2019).

The Rapid-refresh Multiscale Analysis and Prediction System-Short Term (RMAPS-ST) is a Weather Research and Forecasting (WRF) model-based operational regional short-range NWP system developed by the Institute of Urban Meteorology, China. RMAPS-ST focuses on producing fine-scale weather forecasts for North China, towards satisfying the urgent need for meteorological services demanded by those involved in various social activities, as well as disaster prevention and mitigation. The precipitation as well as 2-m temperature and humidity forecasts that it produces are important for economic development and people's daily lives. As mentioned above, NRT GVF is potentially advantageous for weather and climate forecasting. However, the above studies only assessed NRT GVF in the LSM, in regional climate models, in terms of regional weather (but only as case studies), or in global models for long-term validation (such as ECMWF IFS), with relatively few studies having been carried out on the effects of NRT GVF on short-term weather forecasts over North China with a high-resolution (3-km) weather model. To this end, the aim of the present study is to improve our understanding on the impact of NRT GVF on short-term regional weather forecasts by comparing an NRT GVF dataset against the monthly climatological GVF with the WRF model.

Moreover, the simulations cover the whole year in order to analyze the impacts of different seasons. Such a detailed assessment of the influence of NRT GVF data on NWP is necessary for procedural updates in operational forecast systems.

Additionally, many studies have focused on the positive effects of NRT GVF on 2-m temperature forecasts; however, as one would expect, there are also some negative impacts. Hence, the regions affected by these negative impacts are also discussed in this study. Previous studies have indicated that the initialization of soil moisture is the important component in the interactions between the land surface and atmosphere, and that the soil moisture could affect the near-surface air temperature owing to its control of the surface energy budget (Huang et al., 1996; Davis et al., 1999; Marshall et al., 2003; Reeves et al., 2011; Massey et al., 2014; Dy and Fung, 2016; Lin and Cheng, 2016). Clearly, accurate representation of the initial soil moisture in NWP models is vital for the calculation of surface fluxes and subsequent forecasts of atmospheric variables. Therefore, the joint action of using NRT GVF and the initial soil moisture is studied here.

2. Data and methods

2.1 GVF datasets

The climatological GVF dataset provided by the WRF model before April 2013 is based on a 5-yr averaged normalized difference vegetation index with a horizontal resolution of roughly $0.144^\circ \times 0.144^\circ$ for each month of the years in the 1990s (Gutman and Ignatov, 1998). Since then, a new dataset with higher resolution has emerged. In April 2013, another climatological GVF dataset was introduced in version 3.5 of WRF (https://www2.mmm.ucar.edu/wrf/users/wps_files/wpsv3.5/updates-3.5.html). This GVF dataset is a 10-yr (2001–2010) averaged monthly dataset derived from MODIS at a resolution of $0.008^\circ \times 0.008^\circ$. In addition, this 10-yr climatological GVF dataset has been set as the default GVF input in version 3.8 WRF since April 2016.

The NRT GVF dataset used in this study is produced by the Institute of Geographic Sciences and Natural Resources Research, Chinese Academy of Sciences. It is computed based on the 8-day, 1-km MODIS vegetation index dataset by following the method proposed by Gutman and Ignatov (1998). In addition, a new cloud mask method (Liu and Liu, 2013) has been introduced in the computing process to reduce the cloud contamination in the GVF data. In this study, the 8-day NRT GVF data from 2001 to 2012 are employed.

2.2 Experimental design

The total annual precipitation of 2012 was the largest in 35 yr over North China (CMA, 2013), while the heaviest daily rainfall of the last 6 decades occurred in Beijing on 21 July 2012, with a record-breaking amount of 460 mm (Zhang et al., 2013). The year 2012 was a wet year, and it is used here to study the influence of GVF on weather forecasting. To evaluate the impact of NRT GVF on land surface–atmosphere interaction, daily 24-h forecasts initialized from 0000 UTC 1 January to 31 December 2012 were run. In this study, we focus on short-range forecasts. Based on the WRF model (version 3.8.1) and Noah LSM (Chen and Dudhia, 2001), two numerical experiments were designed to investigate to what extent NRT GVF can improve the model results. Experiment NRT used the 8-day NRT GVF, while experiment DEFAULT used the MODIS 10-yr monthly climatological GVF provided by the WRF model itself. The experiments were conducted by using a nested configuration of the WRF model. The domain settings, as well as the physical and dynamic configuration of the experiments, were consistent with RMAPS-ST. The outer domain encompasses the whole of China at a spatial resolution of 9 km, while the inner domain is centered at Beijing (40°N , 116°E), covering North China at 3-km grid spacing (Fig. 1). The physical parameterization schemes were the same in the two experiments, including the Rapid Radiative Transfer Model for GCMs radiation scheme for both longwave and shortwave radiation, Thompson double-moment bulk microphysics scheme, and Yonsei University planetary boundary layer scheme. In the outer domain, the Kain–Fritsch cumulus scheme was used. The analysis of the results focuses on the inner domain. The initial and boundary conditions of the experiments are from ECMWF forecast at 0.25° grid spacing and a 3-h time interval. All the experiment runs started from 0000 UTC.

2.3 Model evaluation data

Validation of the forecasts is important for fully understanding the effects of green vegetation cover on the exchange of energy between the land and atmosphere. Unfortunately, it is currently not possible to make comparisons with observational data to justify the energy budget partitioning process, owing to the fact that flux observations are extremely rare. Therefore, in this study, we use other types of surface observations, such as 2-m air temperature, 2-m humidity, and 10-m wind speed, to verify the forecast results. The hourly surface observational data used for evaluating the model performance are from the China meteorological data sharing system.

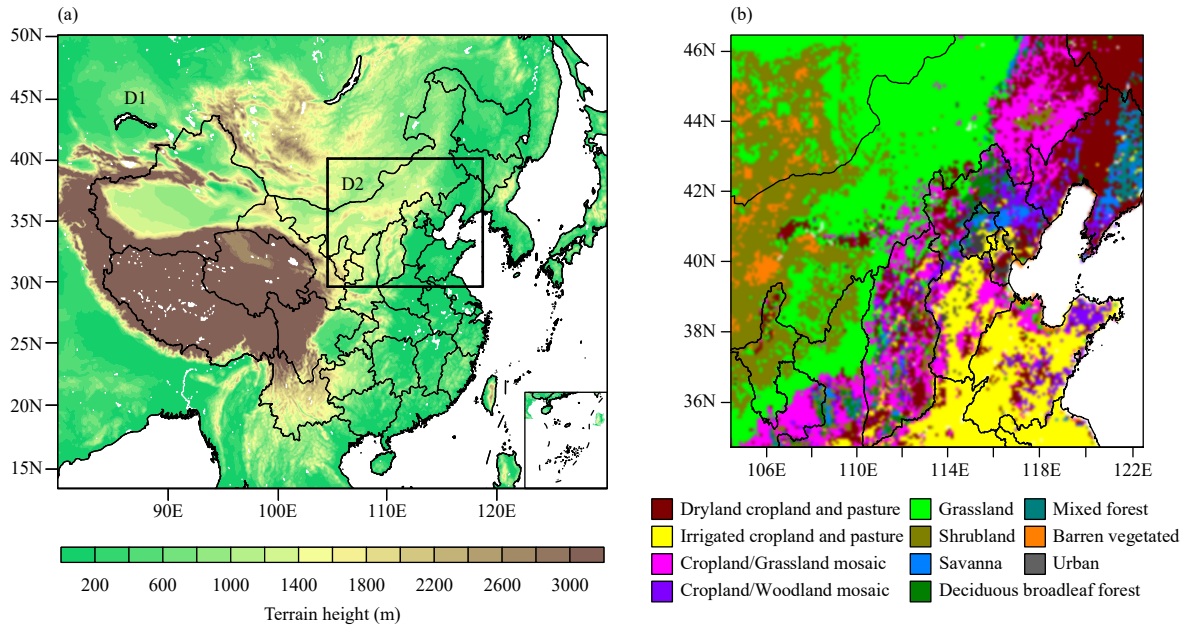


Fig. 1. (a) The two nested model domains used in the WRF forecasts overlaid with topography and (b) land cover map for the 3-km domain.

Specifically, there are 742 surface observation stations in the inner domain. The variables include pressure, 2-m temperature, 2-m specific humidity, and 10-m wind direction and speed. These observation stations are well-distributed over the inner domain and over each type of land cover. The 742 surface stations are the national basic meteorological stations whose observational data quality is reliable. Assessment of the impact of NRT GVF is carried out for the screen-level variables by using two metrics: bias and root-mean-square error (RMSE). These metrics are widely used for evaluating model forecasts.

3. Results

3.1 NRT GVF versus WRF climatological GVF

Before evaluating the model performance by using NRT GVF against the multiyear averaged data, the differences between the 8-day NRT GVF and the 10-yr averaged monthly climatological GVF during the analysis period are first examined. Figure 2 shows the spatial distribution of the 10-yr averaged climatological GVF, NRT GVF, and their difference in the inner domain on 15 April 2012 (during the initial period of vegetation growth) and 15 August 2012 (the peak of vegetation growth). In April, as the vegetation of croplands and forests start to grow, GVF increases gradually. Meanwhile, the barren grasslands result in very low GVF in the northwest of the domain. The difference between the two datasets is clear in the cropland/grassland mosaic areas, and the new 8-day NRT GVF tends to be larger than the climatological GVF with a magnitude between

0.1 and 0.2. A smaller difference is apparent for irrigated cropland and forest, and there is almost no difference for grassland and shrubland. By contrast, as the GVF reaches its peak in August, the difference is larger than that in other months. Notably, the difference reaches as high as 0.3 over grassland. The difference in GVF over the cropland/grassland mosaic and the dryland/cropland mosaic is also significant, reaching 0.2, while the difference over irrigated cropland in August is moderately smaller than that in April. The differences between the 8-day NRT GVF and the 10-yr averaged monthly climatological GVF over the outer domain, which encompasses the whole of China, are more diverse than those over the inner domain (figure not shown). The differences between these two datasets are negligible over eastern China in summer.

The four most distinctive vegetation types that together cover the majority of the inner domain—namely, grassland, irrigated cropland, dryland cropland, and cropland/grassland mosaic—are selected to further compare the NRT GVF and default GVF in detail. Figure 3 reveals the daily variations of these four vegetation types in the two GVF datasets, averaged by the grid cells with the same vegetation type. The daily value of the default monthly GVF is derived from linear interpolation between the two nearby months (based on the method in WRF), while the daily value of the 8-day NRT GVF is kept the same within the 8-day period until the next update. The two datasets are produced by different institutes, so the processes themselves could also introduce the difference. To identify the contribution, the NRT

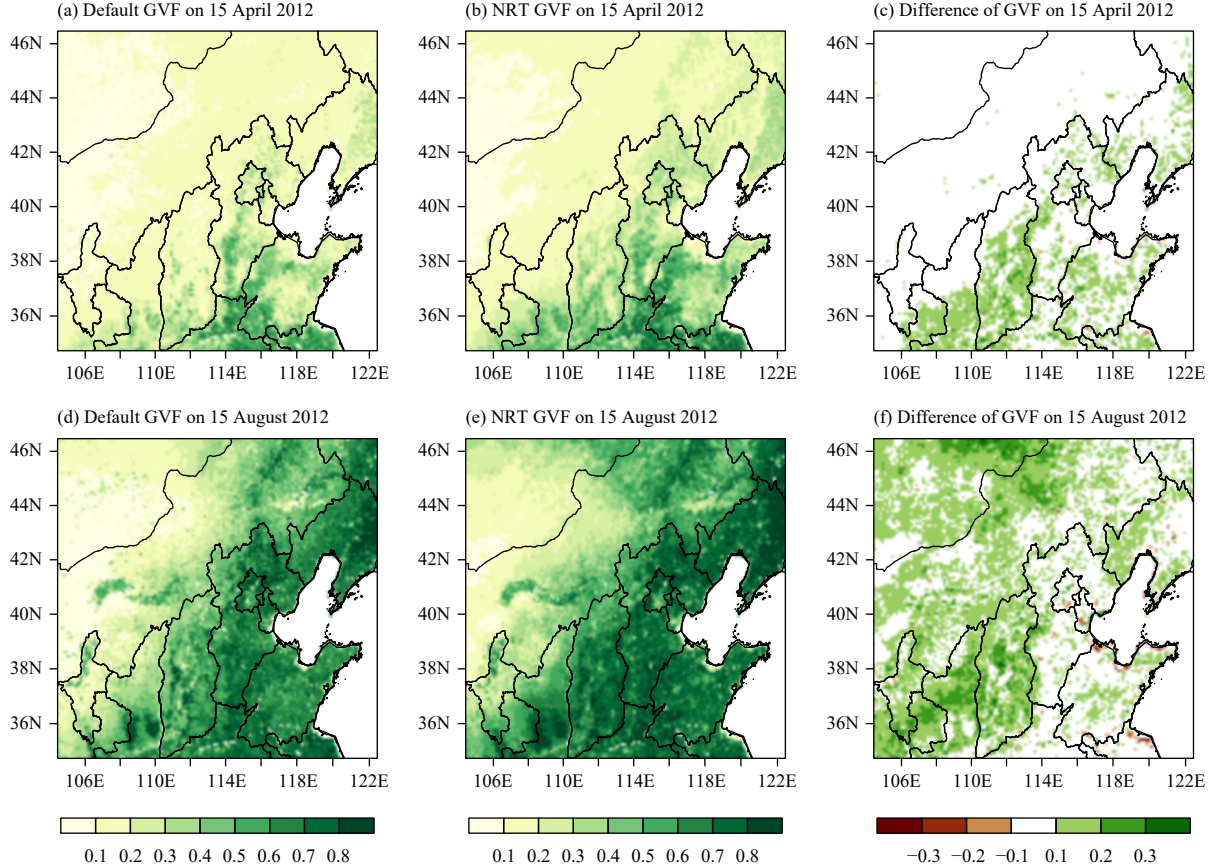


Fig. 2. (a) The 10-yr averaged climatological GVF provided by WRF (default GVF), (b) NRT GVF, and (c) their differences on 15 April 2012. (d–f) are the same as (a–c) but for 15 August 2012.

GVF dataset during 2001–2010 (the time span for WRF's default GVF) is also presented by using the minimum and maximum values (gray shaded area in Fig. 3).

Although the general pattern of annual cycles is similar for both GVF datasets, the differences between the two datasets are distinct. The NRT GVF is higher throughout the year than the default climatological GVF. Most of the time, the minimum NRT GVF during 2001–2010 is higher than the default GVF for the four vegetation types, especially over dryland, grassland, and their mosaic with low vegetation during the cold season. This implies that the data product processes take a small fraction in the difference between the NRT and the default monthly climatological GVF. However, more significantly, the NRT GVF in 2012 is higher than the maximum NRT GVF during 2001–2010 over dryland, grassland, and their mosaic, especially in the warm season. Over the irrigated cropland, the difference between the two datasets is smaller than that over other vegetation types. One possible reason might be that artificial irrigation of agricultural land has consistently affected GVF year on year. The surface vegetation anomalies are strongly related to the cumulative precipitation anom-

alies, especially in semiarid areas. The high GVF during the vegetation growth period (from July to October) of 2012 is strongly related to the stronger precipitation in 2012, demonstrating that 2012 was a wetter-than-normal year over North China. The above results confirm that NRT-updated information on surface vegetation can represent the variations in GVF realistically and may well be able to capture the interannual variability of GVF. Hence, usage of NRT GVF in numerical models is justified. If NRT GVF can change the surface energy partitioning, it may provide better surface variable forecasts as well as better precipitation forecasts.

3.2 Impact of NRT GVF on surface energy fluxes

In the Noah LSM, the surface energy balance is primarily determined by the LH, sensible heat flux (HFX), and ground heat flux (GRDFLX). According to Chen and Dudhia (2001), the LH consists of three components: direct evaporation from the top shallow soil layer (E_{dir}), evaporation of precipitation intercepted by the canopy (E_c), and transpiration via canopy and roots (E_t). That is,

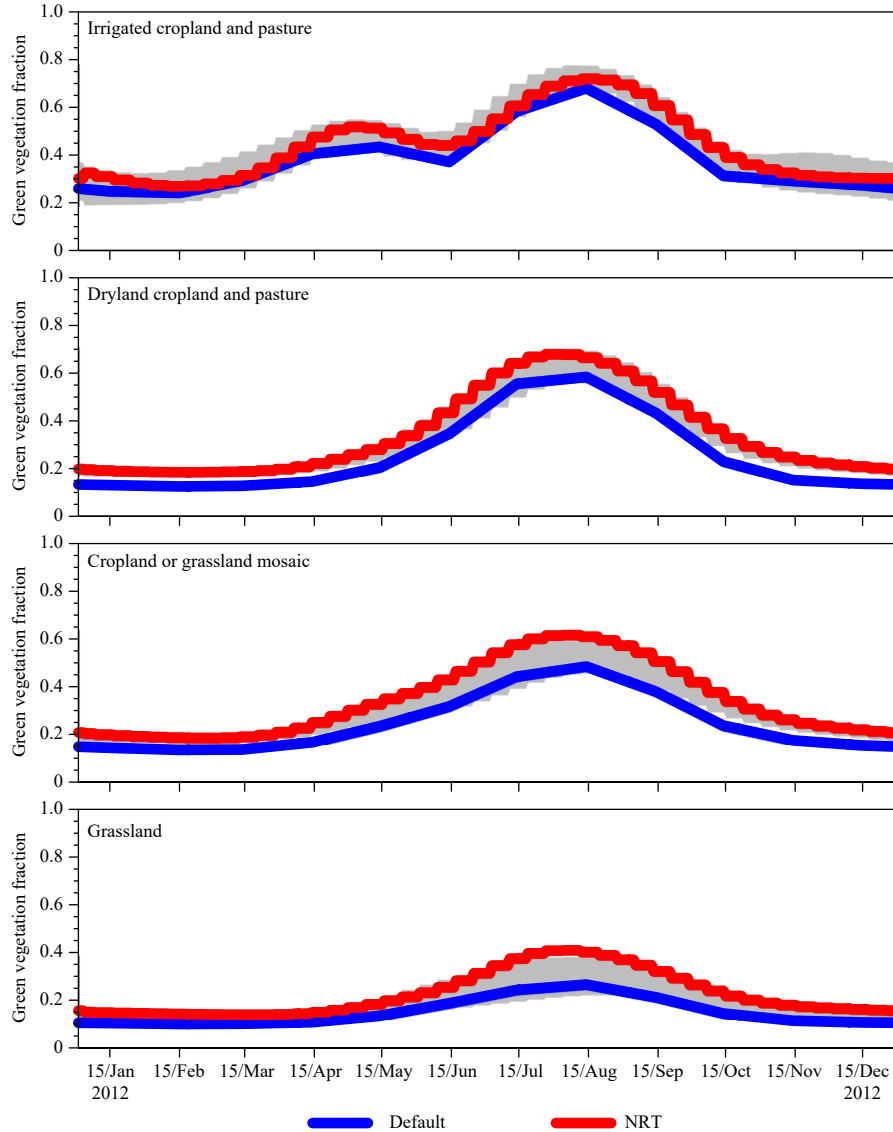


Fig. 3. Time series of the 10-yr averaged monthly GVF and NRT GVF over four vegetation types. The gray shaded area represents the minimum and maximum values of the NRT GVF dataset range from 2001 to 2010.

$$LH = E_{\text{dir}} + E_c + E_t. \quad (1)$$

The canopy evapotranspiration E_t is determined by

$$E_t = \sigma_f E_p B_c \left[1 - \left(\frac{W_c}{S} \right)^n \right], \quad (2)$$

where σ_f is the GVF, E_p is the potential evaporation, B_c is a function of canopy resistance, W_c is the intercepted canopy water content, S is the maximum canopy capacity, and $n = 0.5$. The bare soil evaporation E_{dir} can be written as:

$$E_{\text{dir}} = (1 - \sigma_f) \beta E_p, \quad (3)$$

where β is a function of volumetric soil moisture content and soil hydraulic parameters. In general, both E_t and E_{dir} should increase with the increase in GVF. In contrast,

E_{dir} should decrease because the bare soil fraction is lowered by higher values of GVF. The GVF can also affect GRDFLX as in the Noah LSM, the presence of vegetation could cause a shading effect and a reduction in the soil thermal conductivity. Miller et al. (2006) illustrated how the surface energy balance responds to the variation in GVF. The magnitude of LH increases almost linearly with the increase in GVF, compensated for by a decrease in HFX in the Noah LSM.

The impact of GVF on heat fluxes often shows strong diurnal variations, with the strongest flux appearing in the afternoon. Figure 4 shows the monthly averaged HFX of daytime [0600–0900 UTC averaged, corresponding to local time 1400–1700 Local Standard Time (LST)] in January, April, July, and October, representing winter,

spring, summer, and autumn, respectively. Figure 5 displays the corresponding monthly averaged LH. As the difference between the 8-day NRT GVF and monthly climatological GVF shows annual and regional variations, the impacts of using the NRT GVF on heat fluxes also present temporal and spatial variations. The difference of heat fluxes in January is so small that they can be ignored in the analysis. In the DEFAULT experiment, over the densely vegetated area in the southeast, LH is dominant over HFX, especially over the forest area, while the opposite is observed over the barren vegetated area in the northwest. The difference of surface fluxes between the NRT and the DEFAULT experiments are also displayed in Figs. 4, 5. As a consequence of the increase of GVF in the NRT experiment over North China, an increase in LH and a decrease in HFX are obtained over most parts of the domain during the warm season. These results are physically meaningful since more net radiation is dispersed in the form of latent heat via the enhanced evapotranspiration in response to the increased GVF. The larger variations (exceeding 30 W m^{-2}) in LH and HFX ap-

pear over the cropland/grassland mosaic as well as dryland cropland and grassland areas, where the GVF anomaly is relatively larger. The difference of heat fluxes reaches the largest in July when the GVF reaches its peak, followed by April. Although the LH in October is much smaller than that in July and April, the difference is distinct. The impact of GVF on heat fluxes is much smaller at nighttime because of the absence of solar radiation, and then the impact increases following sunrise. The difference of surface fluxes between the NRT and DEFAULT experiments is clear during the following morning, but to a lesser extent (figure omitted).

In WRF, 2-m air temperature is calculated from the surface temperature and HFX, while 2-m water vapor is calculated from the surface water vapor and LH. Corresponding to the variations of LH and HFX, the NRT GVF decreases the surface temperature and increases the surface water vapor over most regions during daytime. In general, the large differences in 2-m temperature (reaching -0.5°C) and 2-m specific humidity (reaching 0.5 g kg^{-1}) are found over the southwest of the domain where

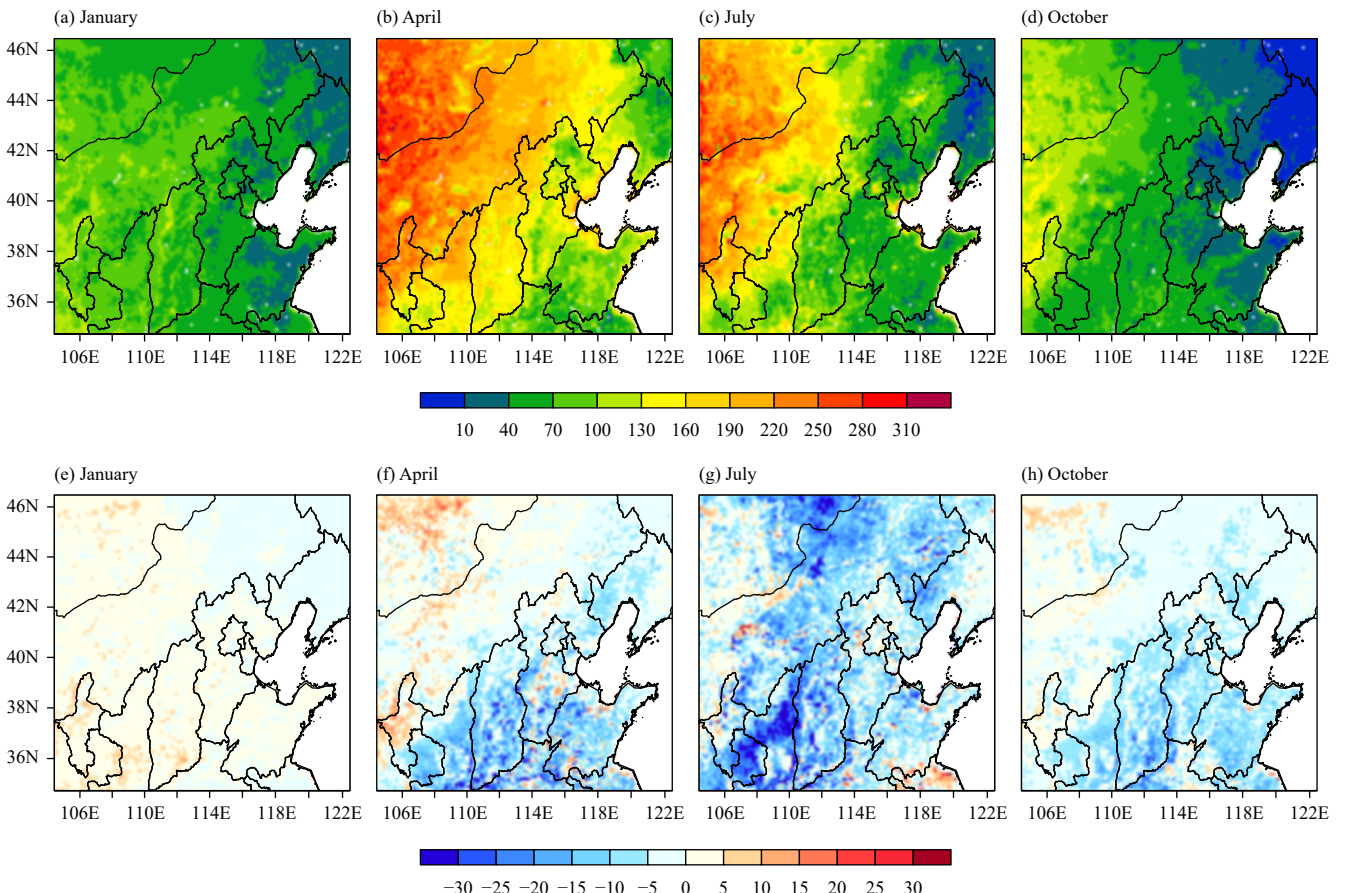


Fig. 4. The monthly afternoon (0600–0900 UTC) surface sensible heat flux ($\text{HFX}; \text{W m}^{-2}$) in the DEFAULT experiment for (a) January, (b) April, (c) July, and (d) October; as well as the difference of HFX between the NRT and DEFAULT experiments for (e) January, (f) April, (g) July, and (h) October.

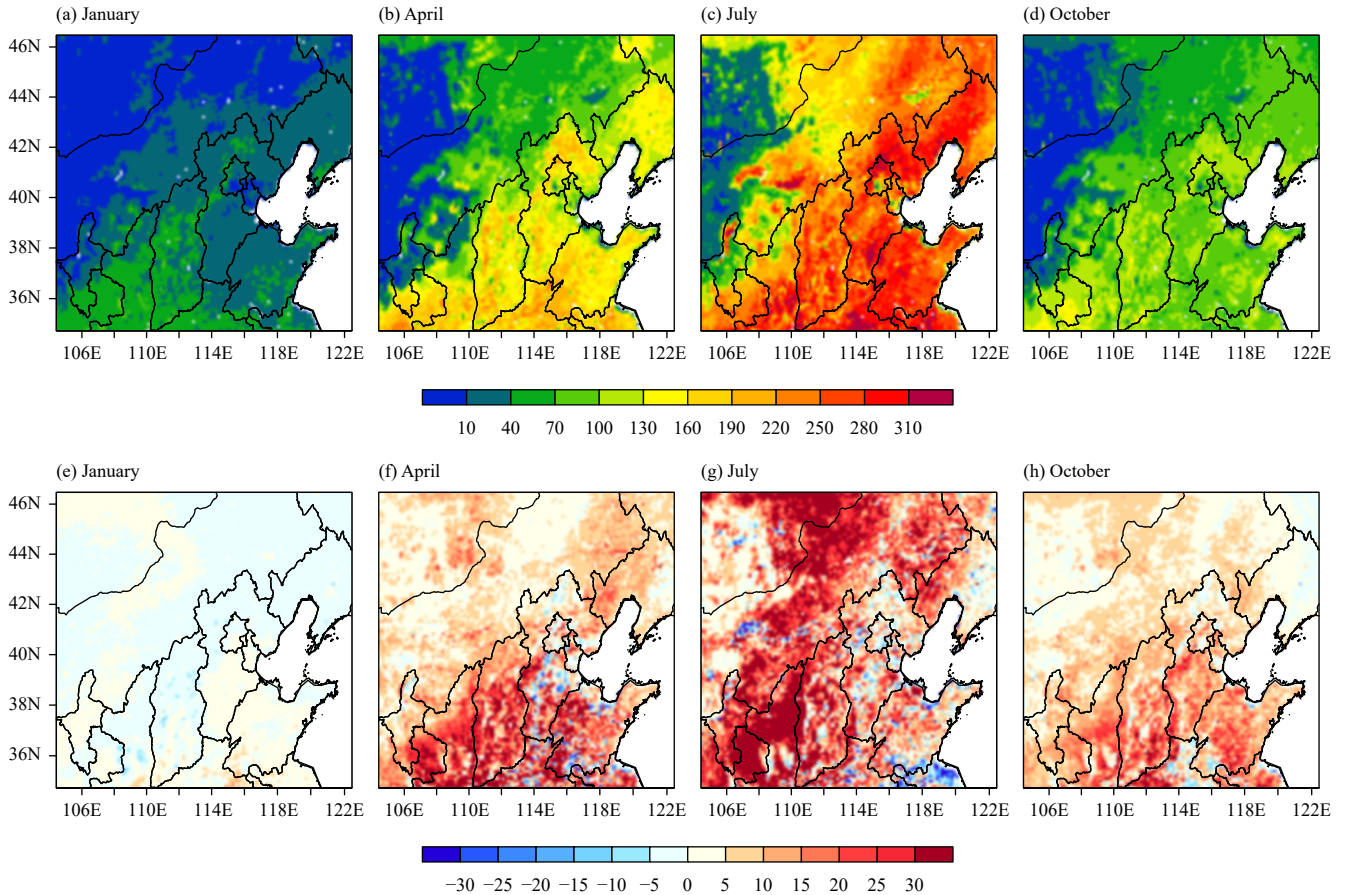


Fig. 5. As in Fig. 4, but for the surface latent heat flux (LH; W m^{-2}).

the GVF variation is relatively larger. The general trends of 2-m temperature difference, as well as its magnitude, match well with the difference in GVF: the larger the difference between the NRT and default GVF, the larger the difference in the 2-m temperature forecast. Similarly, the difference in 2-m humidity is also consistent with the GVF anomaly. The temporal and spatial variations of 2-m temperature are shown in the next section.

3.3 Model evaluation

The model forecasts of 2-m temperature, 2-m specific humidity, and 10-m wind speed from the DEFAULT and NRT experiments were validated by surface observations in terms of bias and RMSE day by day. In the DEFAULT experiment, 2-m temperature biases at 0900 UTC (1700 LST) for April, July, and October are shown in Figs. 6a–c. There is a warm bias in the 2-m temperature forecast in the afternoon. The warmest bias of 2-m temperature appears on the plains with irrigated crop land from spring to autumn. On the plains, the warm biases are serious in April and July, exceeding 1 and 0.5°C at most observation sites, respectively, before then becoming weak in October. Cold biases appear around the

northeastern mountains throughout the year, but more seriously in October than in April and July. The sites located around the western mountains show cold biases in April and October, but warm biases in July. Figures 6d–f display the differences in 2-m temperature between the NRT and DEFAULT experiments. Due to the decrease in HFX in the NRT experiment, most observation sites show a negative effect on 2-m temperature, and this negative effect is more apparent over the plain areas than that over the mountain areas. The warm biases on the plain areas weaken when the NRT GVF is used. The warm biases in daytime in July decrease, but the cold biases over the mountain areas increase in April and October.

Moreover, it is apparent that there is an obvious warm bias the following morning (0800 LST, 24-h forecast). The 2-m temperature 24-h forecast bias in the DEFAULT experiment is shown in Figs. 7a–c. The serious warm biases are around the domain, especially in the mountain areas. Figures 7d–f display the difference in 2-m temperature between the NRT and DEFAULT experiments in 24-h forecasts. Similarly, the warm biases at sunrise are weakened.

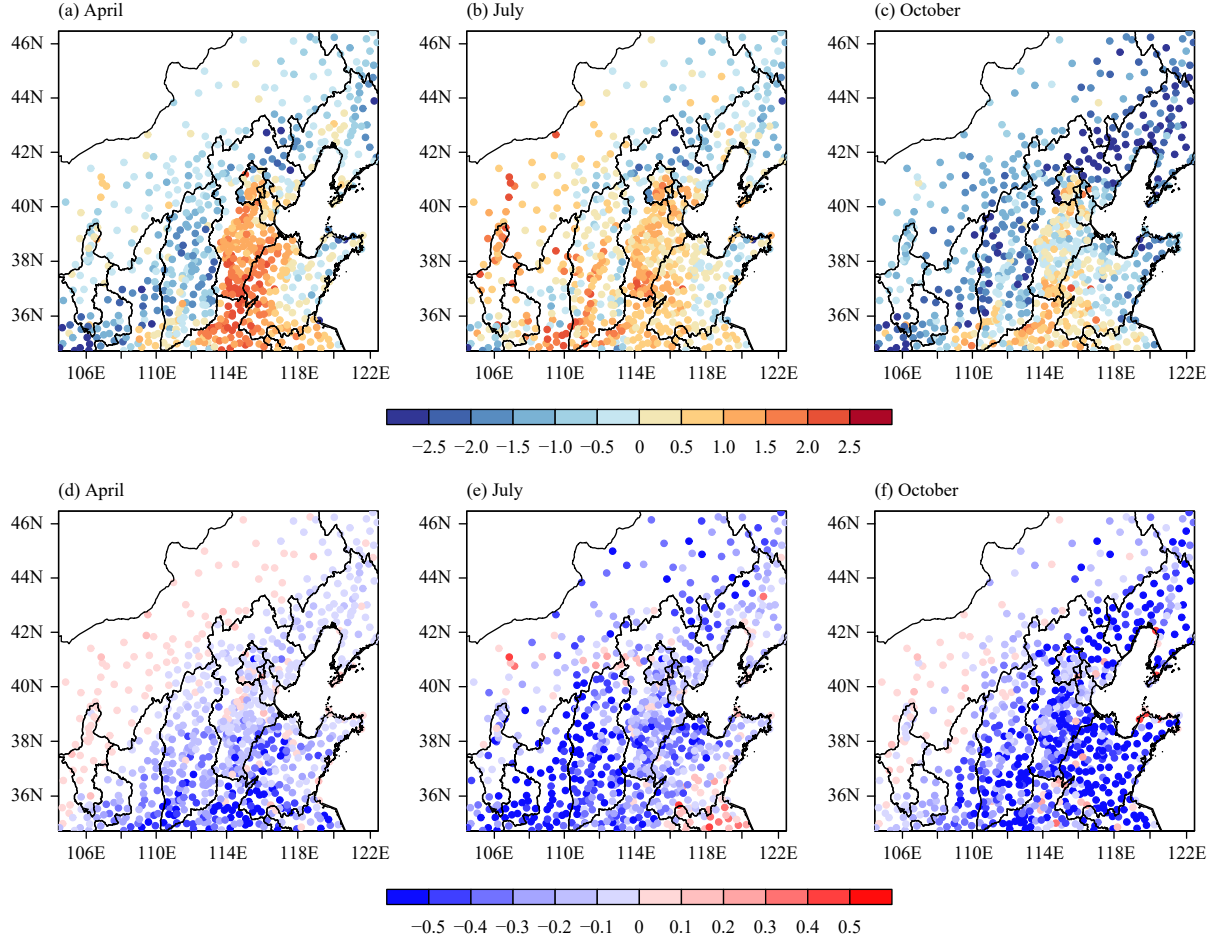


Fig. 6. The monthly afternoon (0900 UTC) 2-m temperature forecast bias ($^{\circ}$ C) in the DEFAULT experiment for (a) April, (b) July, and (c) October; as well as the difference in 2-m temperature bias between the NRT and DEFAULT experiments for (d) April, (e) July, and (f) October.

The monthly averaged biases and RMSE for 2-m temperature in the whole inner-domain from April to October are shown in Table 1. In the afternoon (1700 LST), due to the decrease in the warm bias over the plain areas, the RMSE of 2-m temperature decreases from April to July when the NRT GVF is used. However, the warm bias in the DEFAULT experiment becomes weaker from August, while the cold bias enlarges over the mountain areas and the RMSE increases slightly. In the following morning (0800 LST), the RMSE is reduced from April to October when the NRT GVF is used, resulting from the decrease in the warm bias in the mountain areas. In addition, according to Boussetta et al. (2015), the quantitative impact of using NRT GVF on 2-m temperature can be defined as below:

$$\text{Impact}(T_{2m}) = \text{RMSE}(T_{2m_{\text{NRT}}}) - \text{RMSE}(T_{2m_{\text{DEFAULT}}}), \quad (4)$$

where subscript “NRT” refers to the NRT GVF-based forecast and the subscript “DEFAULT” to the climatological-GVF based forecast. Therefore, a negative (positive) value of the impact means a decrease (increase) in

the 2-m temperature error in comparison with the DEFAULT experiment. The impact of the NRT experiment on the 24-h forecast is displayed in Fig. 8. The observation stations where the RMSE difference of 2-m temperature is less than 0.1° C are ignored in the analysis. The use of NRT GVF generally results in a positive impact on the 2-m temperature forecast in each of the 7 months analyzed here. The RMSEs of most stations have reduced to varying degrees, while fewer stations have experienced negative impacts for the 2-m temperature forecast. From May to July, the most noticeable positive impact occurs in the southwest of the domain, with a magnitude of RMSE reduction on the order of 0.5° C. In other months of the warm season (April, August, September, and October), the most noticeable positive impact also appears in the southwest region, but with the RMSE reduction in a magnitude generally less than 0.3° C. Note that the negative impact on 2-m temperature (less than 0.3° C) mainly occurs in the eastern region of the domain in September over the irrigated cropland or cropland mosaic. In addition, no apparent in-situ valida-

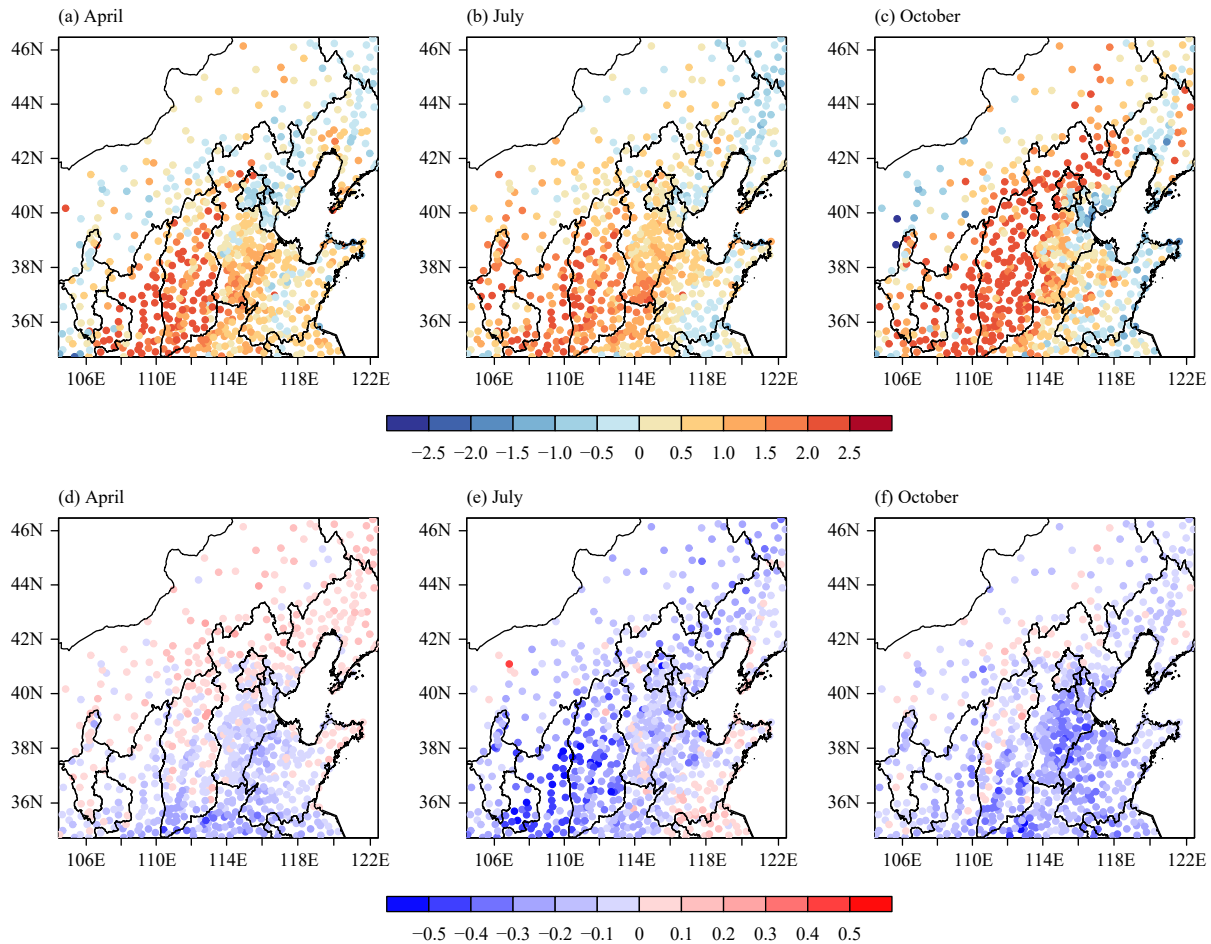


Fig. 7. As in Fig. 6, but for 0000 UTC.

Table 1. Evaluation of monthly surface variable forecasts in the DEFAULT (in parentheses) and NRT experiments (the boldface value means the positive impact)

Month	9-h forecast						24-h forecast					
	2-m temperature		2-m specific humidity		10-m wind speed		2-m temperature		2-m specific humidity		10-m wind speed	
	Bias	RMSE	Bias	RMSE	Bias	RMSE	Bias	RMSE	Bias	RMSE	Bias	RMSE
April	0.10(0.12)	2.01 (2.04)	0.48(0.04)	1.24(1.11)	1.47(1.56)	2.42 (2.49)	0.71(0.83)	2.13 (2.23)	0.11(-0.18)	1.19 (1.21)	1.57(1.66)	2.48 (2.58)
May	0.14(0.57)	2.06 (2.15)	0.20(-0.49)	1.71 (1.74)	1.37(1.45)	2.27 (2.34)	0.83(1.18)	2.01 (2.22)	-0.25(-0.79)	1.56 (1.75)	1.20(1.31)	2.08 (2.21)
June	0.06(0.37)	2.21 (2.23)	0.55(0.18)	1.65(1.53)	1.44(1.52)	2.39 (2.46)	0.94(1.13)	2.00 (2.14)	-0.03(-0.29)	1.33 (1.37)	1.21(1.29)	1.98 (2.06)
July	0.09(0.42)	2.07 (2.18)	0.93(-0.07)	2.11(1.94)	1.31(1.42)	2.14 (2.24)	0.57(0.73)	1.72 (1.84)	0.30(-0.24)	1.58 (1.68)	1.26(1.33)	2.00 (2.09)
August	-0.53(-0.26)	1.75(1.67)	1.16(0.79)	2.04(1.82)	1.22(1.26)	1.91 (1.94)	0.11(0.49)	1.75 (1.88)	0.13(-0.21)	1.46 (1.55)	1.20(1.22)	1.94 (1.96)
September	-0.70(-0.65)	1.87(1.81)	1.17(0.74)	1.84(1.54)	1.04(1.15)	1.80 (1.88)	0.35(0.58)	1.93 (1.97)	-0.16(-0.30)	1.19 (1.23)	1.20(1.25)	1.93 (1.98)
October	-0.85(-0.73)	2.12(2.04)	0.38(0.61)	0.70 (1.29)	1.18(1.19)	1.91 (1.92)	0.92(1.08)	2.32 (2.35)	-0.27(-0.39)	1.05 (1.09)	1.52(1.09)	2.17 (2.25)

tion can be found over the northeastern part of Inner Mongolia, where an unequal pattern of differences in HFX is shown in Fig. 4. This is simply because of the sparseness of observation sites in this region.

Similarly, an evaluation of 2-m specific humidity is shown in Table 1. Due to the partitioning of surface HFX and LH, in the DEFAULT experiment, the warm bias has a positive correlation with the dry bias, while the cold bias has a positive correlation with the wet bias (figure omitted). The impact on the surface humidity displays a similar pattern to that on temperature. From April to July, the dry bias can be improved by using NRT GVF, but the

wet bias enlarges from August to October in the afternoon. In the morning, dry biases appear at most observation sites from April to October in the DEFAULT experiment, while NRT can reduce the dry biases.

In WRF, the surface roughness is critical in the calculation of surface wind speed, and GVF is one of the factors needed for calculating the surface roughness. The bias of 10-m wind speed is shown in Table 1, from which we can see that there is an obviously positive bias for the surface wind speed forecast. If the GVF in NRT is higher than that in DEFAULT, the surface roughness increases, and the wind speed bias decreases. The forecast error of

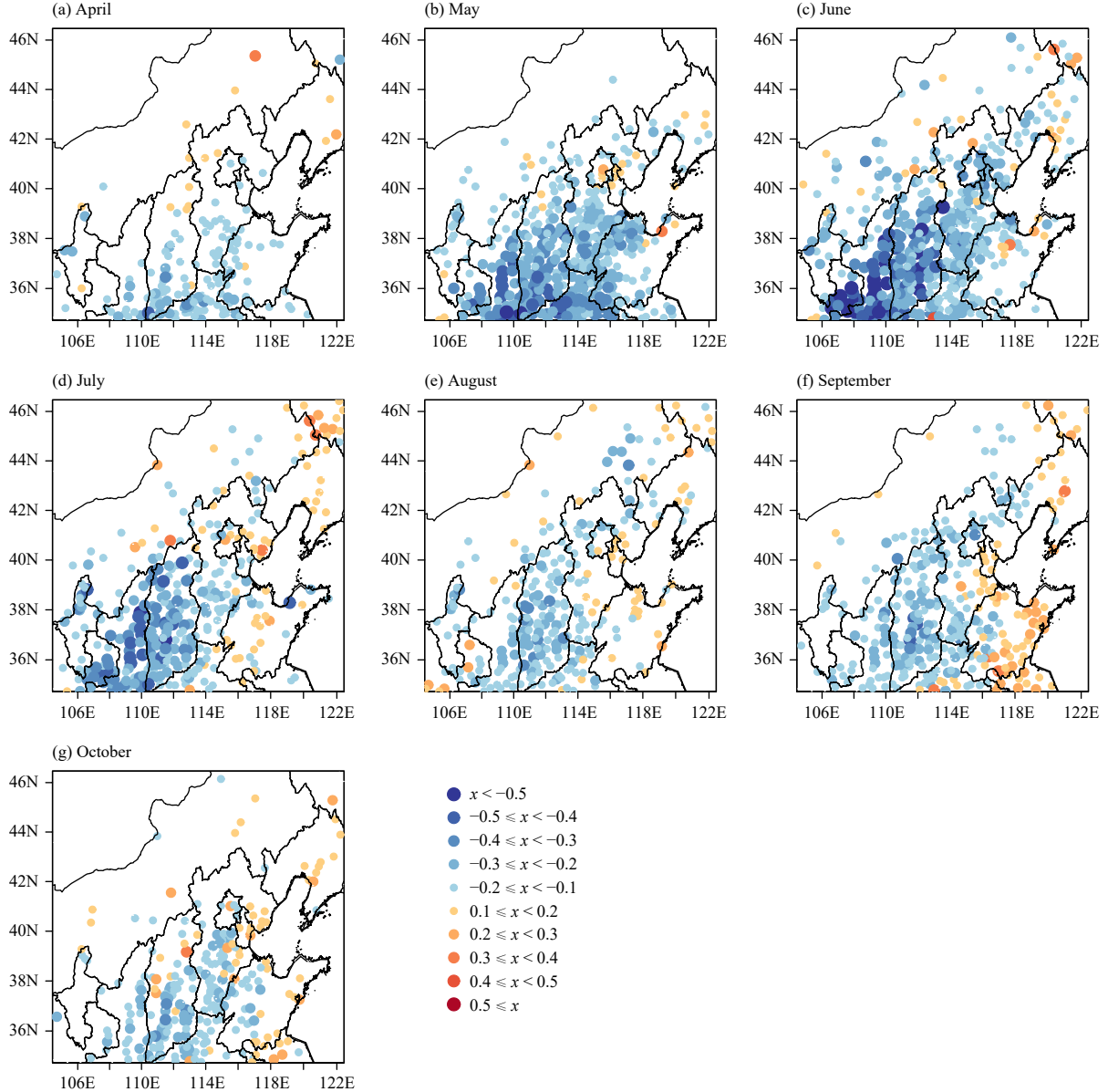


Fig. 8. Monthly averaged scores of the forecast experiment using NRT GVF (NRT) against the experiment using the climatology (DEFAULT) for 24-h forecasts of 2-m temperature. A negative (positive) value means a reduction (increase) in the forecast RMSE against in-situ observations.

10-m wind speed has been improved slightly by using NRT GVF. Based on the statistical analysis in Table 1, the average RMSEs for the 9-h (afternoon) forecast of 2-m temperature and 10-m wind speed in the domain from April to October have declined by 0.5% and 3%, respectively. However, the RMSEs for 2-m specific humidity have increased by 2%. The RMSEs for the 24-h (morning) forecast of 2-m temperature, 2-m specific humidity, and 10-m wind speed have declined by 5%, 6%, and 4%, respectively.

3.4 Impact on precipitation

In the model integration, precipitation forecasting in-

volves complex nonlinear processes. The averaged accumulative precipitation of the two experiments and their differences are presented in Fig. 9. The effect of GVF on the precipitation pattern in the forecast is minimal, but a difference in the amount of precipitation is apparent. In general, there is more precipitation (increment of 8%) in the NRT experiment, over the grassland, dryland crop-land, cropland and grassland mosaic areas. The pattern of increase in precipitation follows that of GVF in Fig. 2f, as well as that of LH in Figs. 5f–g. These results illustrate that higher GVF causes an increase in the upward moisture flux from the surface to atmosphere, resulting in more precipitation. Besides the average daily precipita-

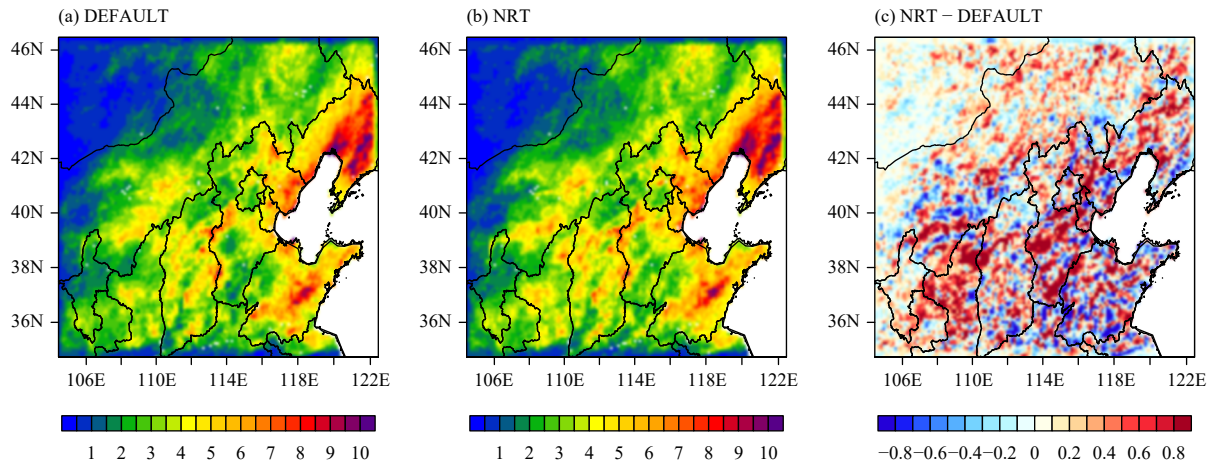


Fig. 9. The averaged 24-h accumulative precipitation (mm day^{-1}) from 1 June to 31 August: (a) DEFAULT experiment, (b) NRT experiment, and (c) NRT experiment minus DEFAULT experiment.

tion, each rainfall case was compared between the two experiments, but a meaningful summary in this regard was difficult to achieve. The impact of NRT GVF on precipitation should be analyzed in detail in future work.

4. Negatively-impacted regions

As presented in Figs. 6, 7, using NRT GVF can bring cold and wet biases. As shown in Fig. 8, there are moderate negative impacts on 2-m temperature over the northeast and other regions from April to October, particularly over the eastern regions and during September. More specifically, for the 24-h 2-m temperature forecast, the negatively-impacted stations account for 16%, while the in-situ stations where the difference of RMSE is less than 0.1°C can be ignored. Nonetheless, overall, it is worthwhile to investigate the causes of the negative impact.

Although there is an overall warm bias over North China, most of the negatively-impacted stations in the DEFAULT experiments show small warm or small cold biases. The mean bias of the 24-h 2-m temperature forecast for all stations is 0.8°C , while the mean bias for negatively-impacted stations is -0.1°C . These stations are mostly located in the forest and nearby areas, where LH is dominant (Figs. 4, 5). As the soil moisture plays an important role in the partitioning of HFX and LH, the wet soil moisture leads to more soil water being evaporated from the top shallow soil layer to the atmosphere, favoring more upward LH and less HFX. The effect of soil moisture is similar to that of GVF in the partitioning of heat fluxes. Therefore, the overlying effects of soil moisture and GVF need to be considered. As shown in Fig. 10, the LH-dominant area corresponds to the wet-soil-moisture areas. Based on thorough comparative analysis,

we find that most negatively-impacted stations are situated in areas with larger soil moisture.

4.1 Initial soil moisture condition

As thermodynamic properties of the atmospheric boundary layer are always related to the soil moisture, it might be possible to tune soil variables to compensate for various model biases (Di Giuseppe et al., 2011). Being highly dependent on the atmospheric model formulation, soil moisture from one model might not be applicable in another model. The initial soil moisture fields for the DEFAULT and NRT experiments were also provided by ECMWF's operational IFS. As shown in the ECMWF's evaluation of soil moisture by using global ground-based in-situ observations, the IFS shows good skills in capturing the surface soil moisture variability, but tends to overestimate the quantity of soil moisture, particularly in dryland areas (Albergel et al., 2012). These wet biases are also present over North China.

To study the biases in soil moisture initialization, the monthly averaged initial top 10-cm soil moisture (hereafter referred to as surface soil moisture) from the simulations were evaluated by using 372 ground-based in situ observations. The results are consistent with ECMWF's evaluation, and the soil moisture in the initial conditions is overestimated throughout the year (Table 2). The wettest bias is in January, reaching 0.14 m m^{-3} . However, it should be noted that most soil moisture devices have the potential to malfunction when soils are frozen, so the soil moisture measurements may be underestimated (Halilainen et al., 1985). The smallest bias is in spring, at 0.035 m m^{-3} .

The spatial characteristics of the monthly averaged initial surface soil moisture and observations in April, July, and October are shown in Fig. 10. In April, the initial

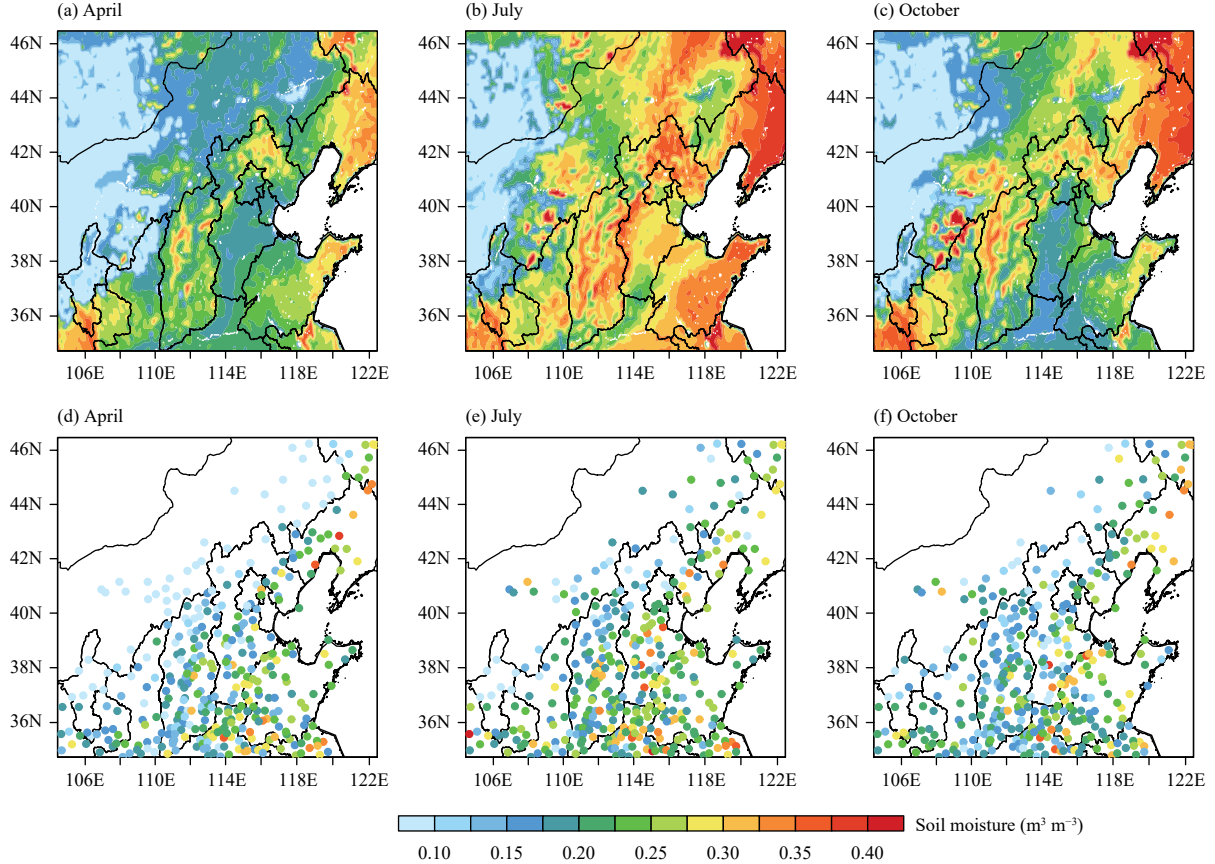


Fig. 10. The monthly initial surface soil moisture for both the experiments (DEFAULT and NRT) in (a) April, (b) July, and (c) October, as well as the observed monthly soil moisture in (d) April, (e) July, and (f) October.

conditions are slightly wetter than in the observations over forest areas. In October, the wet bias grows substantially (with the maximum of 0.043 m m^{-3}), especially over the northeastern and eastern areas, where the negative impacts on 2-m temperature are notable and most of the negatively-impacted areas are cropland. The situation in other months of the warm season is similar.

4.2 Statistics of negative impact

There is a strong correlation between the negative effect on 2-m temperature by using NRT GVF and the initial soil moisture conditions. The correlations among the initial surface moisture conditions, GVF difference, and its effect on the 24-h forecast of 2-m temperature are presented in Fig. 11. The GVF_s at most stations in the NRT experiment are higher than those in the DEFAULT experiment. The growing GVF leads to the increasing LH and decreasing HFX, diminishing the warm bias. The soil moisture displays the same effect. These two factors could reduce the warm bias to such an extent that they cause a negative effect on the 2-m temperature forecast. The statistics demonstrate that half of the negatively-impacted stations have soil moisture larger than 0.3 m m^{-3} ,

Table 2. Biases of initial surface soil moisture conditions

Month	Bias	Month	Bias	Month	Bias
January	0.148	May	0.038	September	0.068
February	0.127	June	0.042	October	0.043
March	0.063	July	0.078	November	0.067
April	0.041	August	0.089	December	0.104

while stations with high moisture only account for 20%. This indicates that using NRT GVF can improve 2-m temperature forecasts at 90% of stations in the low-soil-moisture areas, but 60% of stations in the high-soil-moisture areas. There is no denying that using NRT GVF can improve the 2-m temperature forecast, but the inaccurate initial soil moisture conditions also need to be considered.

5. Conclusions and discussion

Given the importance of vegetation in land-atmosphere interactions, this study evaluated the quality of an NRT GVF dataset by comparing it with the multiyear monthly climatological GVF, and examined their impacts on the surface processes in the WRF model which employs the Noah LSM.

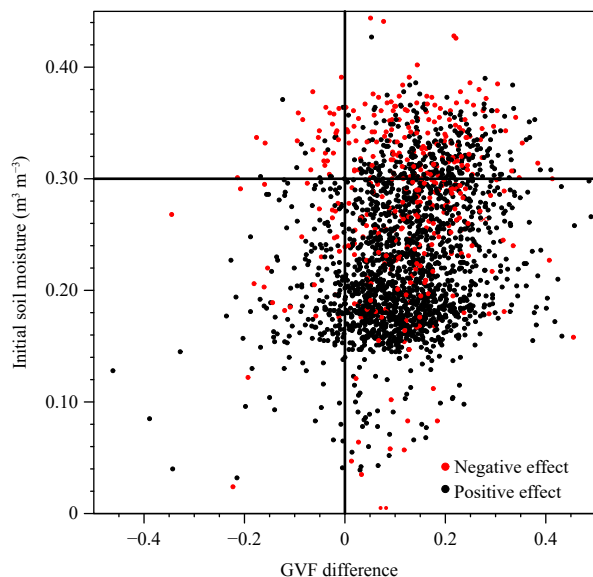


Fig. 11. Scatterplots of the positive and negative effects on 2-m temperature by using NRT GVF. The monthly initial surface soil moisture ($\text{m}^3 \text{m}^{-3}$) is shown on the y-axis, plotted against the GVF difference.

A detailed comparison was made between the NRT GVF and the MODIS 10-yr monthly climatological GVF used in WRF by default. The annual precipitation of North China in 2012 was much more than normal. As surface vegetation anomalies were strongly related to the cumulative precipitation anomalies, the GVF of 2012 was generally higher than other years of the last decade. It was found that the NRT GVF data were able to detect the annual variability of GVF.

The benefit of employing NRT GVF to the prediction of near-surface temperature and humidity was assessed by comparing an experiment by using this dataset with the DEFAULT run. The results demonstrated that the surface fluxes and screen-level variables (temperature and humidity) were sensitive to the usage of NRT GVF. The application of the 8-day NRT GVF in WRF generally increased the LH and decreased the HFX in most regions when compared with the usage of default climatological GVF. Hence, NRT GVF can provide cooler surface temperature and higher surface humidity, reducing warm and dry biases in the afternoon and the following morning during the vegetation growing season.

Evaluation of in-situ observations showed positive impacts on 2-m temperature, 2-m specific humidity, and 10-m wind speed during the daytime. NRT GVF can reduce the warm and dry biases over the plain areas in the afternoon from April to July, and over the mountain areas the following morning from April to October, too. A moderate increase in error appeared in the afternoon from August to October due to overcooling. The NRT GVF can

also improve the surface wind speed forecast. Further analysis demonstrated that the soil moisture influences the moisture flux on the land surface, meaning that the overlying effect of the initial soil moisture conditions and GVF should be considered together. The positive or negative effects of using NRT GVF are closely related to the soil moisture. These findings provide insight into using NRT GVF in operational NWP.

Importantly, this study has shown that there exist several drawbacks to using this NRT GVF dataset derived from MODIS instruments in operational NWP systems in China. However, Han et al. (2020) recently reported that new vegetation products retrieved from the Medium Resolution Spectral Imager-II (MERSI-II) onboard China's Fengyun (FY) satellite (FY-3 series; FY-3D) are consistent with the MODIS data but without systematic biases. Therefore, in the next step for this line of research, it would be worthwhile testing the potential of MERSI-II GVF products for applications in NWP systems. Alongside this, however, several issues raised in the present study also need to be explored further. For instance, although this study has demonstrated improvement in model forecasts by using NRT GVF in a wet-anomaly case with higher GVF in 2012, the performance of the dataset as applied to a drought case should also be examined. Additionally, the structure of low-level temperature and humidity fields may be altered when NRT GVF is used. The effects of using NRT GVF on precipitation forecasts also need to be evaluated in detail in the future.

Acknowledgments. GVF data used in this study are available from the China Meteorological Administration Special Public Welfare Research Fund (GYHY201106014).

REFERENCES

- Abramopoulos, F., 1988: Generalized energy and potential enstrophy conserving finite difference schemes for the shallow water equations. *Mon. Wea. Rev.*, **116**, 650–662, doi: 10.1175/1520-0493(1988)116<0650:GEAPEC>2.0.CO;2.
- Albergel, C., P. De Rosnay, G. Balsamo, et al., 2012: Soil moisture analyses at ECMWF: Evaluation using global ground-based in situ observations. *J. Hydrometeor.*, **13**, 1442–1460, doi: 10.1175/JHM-D-11-0107.1.
- Balsamo, G., A. Beljaars, K. Scipal, et al., 2009: A revised hydrology for the ECMWF model: Verification from field site to terrestrial water storage and impact in the integrated forecast system. *J. Hydrometeor.*, **10**, 623–643, doi: 10.1175/2008JHM1068.1.
- Beljaars, A. C. M., P. Viterbo, M. J. Miller, et al., 1996: The anomalous rainfall over the United States during July 1993. Sensitivity to land surface parameterization and soil moisture anomalies. *Mon. Wea. Rev.*, **124**, 362–383, doi: 10.1175/1520-0493(1996)124<362:TAROU>2.0.CO;2.

- 0-0493(1996)124<0362:TAROTU>2.0.CO;2.
- Boussetta, S., G. Balsamo, A. Beljaars, et al., 2013: Impact of a satellite-derived leaf area index monthly climatology in a global numerical weather prediction model. *Int. J. Remote Sens.*, **34**, 3520–3542, doi: 10.1080/01431161.2012.716543.
- Boussetta, S., G. Balsamo, E. Dutra, et al., 2015: Assimilation of surface albedo and vegetation states from satellite observations and their impact on numerical weather prediction. *Remote Sens. Environ.*, **163**, 111–126, doi: 10.1016/j.rse.2015.03.009.
- Case, J. L., F. J. LaFontaine, J. R. Bell, et al., 2014: A real-time MODIS vegetation product for land surface and numerical weather prediction models. *IEEE Trans. Geosci. Remote Sens.*, **52**, 1772–1786, doi: 10.1109/TGRS.2013.2255059.
- Chen, F., and J. Dudhia, 2001: Coupling an advanced land surface–hydrology model with the Penn State–NCAR MM5 modeling system. Part I: Model implementation and sensitivity. *Mon. Wea. Rev.*, **129**, 569–585, doi: 10.1175/1520-0493(2001)129<0569:CAALSH>2.0.CO;2.
- China Meteorological Administration (CMA), 2013: *China Climate Bulletin 2012*. China Meteorological Administration, Beijing, 56 pp. (in Chinese)
- Crawford, T. M., D. J. Stensrud, F. Mora, et al., 2001: Value of incorporating satellite-derived land cover data in MM5/PLACE for simulating surface temperatures. *J. Hydrometeor.*, **2**, 453–468, doi: 10.1175/1525-7541(2001)002<0453:VOISDL>2.0.CO;2.
- Davis, C., T. Warner, E. Astling, et al., 1999: Development and application of an operational, relocatable, mesogamma-scale weather analysis and forecasting system. *Tellus Dyn. Meteor. Oceanogr.*, **51**, 710–727, doi: 10.3402/tellusa.v51i5.14490.
- Di Giuseppe, F., D. Cesari, and G. Bonafé, 2011: Soil initialization strategy for use in limited-area weather prediction systems. *Mon. Wea. Rev.*, **139**, 1844–1860, doi: 10.1175/2011MWR3279.1.
- Dickinson, R. E., J. A. Berry, G. B. Bonan, et al., 2002: Nitrogen controls on climate model evapotranspiration. *J. Climate*, **15**, 278–295, doi: 10.1175/1520-0442(2002)015<0278:NCOCME>2.0.CO;2.
- Dy, C. Y., and J. C. H. Fung, 2016: Updated global soil map for the Weather Research and Forecasting model and soil moisture initialization for the Noah land surface model. *J. Geophys. Res. Atmos.*, **121**, 8777–8800, doi: 10.1002/2015JD024558.
- Ek, M. B., K. E. Mitchell, Y. Lin, et al., 2003: Implementation of Noah land surface model advances in the National Centers for Environmental Prediction operational mesoscale Eta model. *J. Geophys. Res. Atmos.*, **108**, 8851, doi: 10.1029/2002JD003296.
- Ge, Q. S., X. Z. Zhang, and J. Y. Zheng, 2014: Simulated effects of vegetation increase/decrease on temperature changes from 1982 to 2000 across the Eastern China. *Int. J. Climatol.*, **34**, 187–196, doi: 10.1002/joc.3677.
- Gutman, G., and A. Ignatov, 1998: The derivation of the green vegetation fraction from NOAA/AVHRR data for use in numerical weather prediction models. *Int. J. Remote Sens.*, **19**, 1533–1543, doi: 10.1080/014311698215333.
- Hallikainen, M. T., F. T. Ulaby, M. C. Dobson, et al., 1985: Microwave dielectric behavior of wet soil—Part 1: Empirical models and experimental observations. *IEEE Trans. Geosci. Remote Sens.*, **GE-23**, 25–34, doi: 10.1109/TGRS.1985.289497.
- Han, X. Z., J. Yang, S. H. Tang, et al., 2020: Vegetation products derived from *Fengyun-3D* medium resolution spectral imager-II. *J. Meteor. Res.*, **34**, 775–785, doi: 10.1007/s13351-020-0027-5.
- Huang, J., H. M. Van Den Dool, and K. P. Georgarakos, 1996: Analysis of model-calculated soil moisture over the United States (1931–1993) and applications to long-range temperature forecasts. *J. Climate*, **9**, 1350–1362, doi: 10.1175/1520-0442(1996)009<1350:AOMCSM>2.0.co;2.
- James, K. A., D. J. Stensrud, and N. Yussouf, 2009: Value of real-time vegetation fraction to forecasts of severe convection in high-resolution models. *Wea. Forecasting*, **24**, 187–210, doi: 10.1175/2008WAF2007097.1.
- Jiang, L., F. N. Kogan, W. Guo, et al., 2010: Real-time weekly global green vegetation fraction derived from advanced very high resolution radiometer-based NOAA operational global vegetation index (GVI) system. *J. Geophys. Res. Atmos.*, **115**, D11114, doi: 10.1029/2009JD013204.
- Kogan, F. N., 1997: Global drought watch from space. *Bull. Amer. Meteor. Soc.*, **78**, 621–636, doi: 10.1175/1520-0477(1997)078<0621:GDWFS>2.0.CO;2.
- Koster, R. D., S. P. P. Mahanama, T. J. Yamada, et al., 2010: Contribution of land surface initialization to subseasonal forecast skill: First results from a multi-model experiment. *Geophys. Res. Lett.*, **37**, L02402, doi: 10.1029/2009GL041677.
- Kurkowski, N. P., D. J. Stensrud, and M. E. Baldwin, 2003: Assessment of implementing satellite-derived land cover data in the Eta Model. *Wea. Forecasting*, **18**, 404–416, doi: 10.1175/1520-0434(2003)18<404:AOISDL>2.0.CO;2.
- Lin, T. S., and F. Y. Cheng, 2016: Impact of soil moisture initialization and soil texture on simulated land–atmosphere interaction in Taiwan. *J. Hydrometeor.*, **17**, 1137–1355, doi: 10.1175/JHM-D-15-0024.1.
- Liu, R. G., and Y. Liu, 2013: Generation of new cloud masks from MODIS land surface reflectance products. *Remote Sens. Environ.*, **133**, 21–37, doi: 10.1016/j.rse.2013.01.019.
- Liu, Y., J. B. Wang, J. W. Dong, et al., 2020: Variations of vegetation phenology extracted from remote sensing data over the Tibetan Plateau hinterland during 2000–2014. *J. Meteor. Res.*, **34**, 786–797, doi: 10.1007/s13351-020-9211-x.
- Marshall, C. H., K. C. Crawford, K. E. Mitchell, et al., 2003: The impact of the land surface physics in the operational NCEP Eta Model on simulating the diurnal cycle: Evaluation and testing using Oklahoma Mesonet data. *Wea. Forecasting*, **18**, 748–768, doi: 10.1175/1520-0434(2003)018<0748:TIOTLS>2.0.CO;2.
- Massey, J. D., W. J. Steenburgh, S. W. Hoch, et al., 2014: Sensitivity of near-surface temperature forecasts to soil properties over a sparsely vegetated dryland region. *J. Appl. Meteor. Climatol.*, **53**, 1976–1995, doi: 10.1175/JAMC-D-13-0362.1.
- Miller, J., M. Barlage, X. B. Zeng, et al., 2006: Sensitivity of the NCEP/Noah land surface model to the MODIS green vegetation fraction data set. *Geophys. Res. Lett.*, **33**, L13404, doi: 10.1029/2006GL026636.
- Mu, X. H., T. Zhao, G. Y. Ruan, et al., 2021: High spatial resolution and high temporal frequency (30-m/15-day) fractional

- vegetation cover estimation over China using multiple remote sensing datasets: Method development and validation. *J. Meteor. Res.*, **35**, 128–147, doi: 10.1007/s13351-021-0017-2.
- Reeves, H. D., K. L. Elmore, G. S. Manikin, et al., 2011: Assessment of forecasts during persistent valley cold pools in the Bonneville Basin by the North American Mesoscale Model. *Wea. Forecasting*, **26**, 447–467, doi: 10.1175/WAF-D-10-5014.1.
- Rowell, D. P., and C. Blondin, 1990: The influence of soil wetness distribution on short-range rainfall forecasting in the West African Sahel. *Q. J. Roy. Meteor. Soc.*, **116**, 1471–1485, doi: 10.1002/qj.49711649611.
- Yan, Y., J. P. Tang, G. Liu, et al., 2019: Effects of vegetation fraction variation on regional climate simulation over Eastern China. *Global Planet. Change*, **175**, 173–189, doi: 10.1016/j.gloplacha.2019.02.004.
- Yin, J. F., X. W. Zhan, Y. F. Zheng, et al., 2016: Improving Noah land surface model performance using near real time surface albedo and green vegetation fraction. *Agric. Forest Meteor.*, **218–219**, 171–183, doi: 10.1016/j.agrformet.2015.12.001.
- Zeng, X. B., R. E. Dickinson, A. Walker, et al., 2000: Derivation and evaluation of global 1-km fractional vegetation cover data for land modeling. *J. Appl. Meteor.*, **39**, 826–839, doi: 10.1175/1520-0450(2000)039<0826:DAEOGK>2.0.CO;2.
- Zeng, X. B., P. Rao, R. S. DeFries, et al., 2003: Interannual variability and decadal trend of global fractional vegetation cover from 1982 to 2000. *J. Appl. Meteor.*, **42**, 1525–1530, doi: 10.1175/1520-0450(2003)042<1525:IVADTO>2.0.CO;2.
- Zhang, D. L., Y. H. Lin, P. Zhao, et al., 2013: The Beijing extreme rainfall of 21 July 2012: “Right results” but for wrong reasons. *Geophys. Res. Lett.*, **40**, 1426–1431, doi: 10.1002/grl.50304.
- Zheng, D. H., R. Van Der Velde, Z. B. Su, et al., 2014: Assessment of roughness length schemes implemented within the Noah land surface model for high-altitude regions. *J. Hydrometeor.*, **15**, 921–937, doi: 10.1175/JHM-D-13-0102.1.

Tech & Copy Editor: Meili ZHANG